

Fainter harder brighter softer: a correlation between α_{OX} , X-ray spectral state and Eddington ratio in tidal disruption events

Thomas Wevers^{*}

Institute of Astronomy, University of Cambridge, Madingley Road, CB3 0HA, UK

Accepted 2020 May 19. Received 2020 April 28; in original form 2020 March 31.

ABSTRACT

We explore the accretion states of tidal disruption events (TDEs) using a sample of 7 X-ray bright sources. To this end, we estimate the relative contribution of the disk and corona to the observed X-ray emission through spectral modeling, and assess the X-ray brightness (through α_{OX} , $L_{2 \text{ keV}}$ and $f_{\text{Edd,X}}$) as a function of the Eddington ratio. We report strong positive correlations between α_{OX} and $f_{\text{Edd,bol}}$; $f_{\text{Edd,X}}$ and $f_{\text{Edd,UV}}$; and an anti-correlation for $L_{2 \text{ keV}}$ and $f_{\text{Edd,UV}}$. TDEs at high $f_{\text{Edd,bol}}$ have thermal dominated X-ray spectra and high (soft) α_{OX} , whereas those at low $f_{\text{Edd,bol}}$ show a significant power-law contribution and low (hard) α_{OX} . Similar to X-ray binaries and active galactic nuclei, the transition between X-ray spectral states occurs around $f_{\text{Edd,bol}} \approx 0.03$, although the uncertainty is large due to the small sample size. Our results suggest that X-ray surveys are more likely to discover TDEs at low $f_{\text{Edd,bol}}$, whereas optical surveys are more sensitive to TDEs at high Eddington ratios. The X-ray and optical selected TDEs have different UV and X-ray properties, which should be taken into account when deriving rates, luminosity and black hole mass functions. TDEs around the most massive supermassive black holes are observed in the hard state; this could indicate that TDE evolution is faster around more massive BHs.

Key words: accretion, accretion disks – galaxies:nuclei – tidal disruption events – black hole physics – galaxies:active

1 INTRODUCTION

The geometry through which accretion onto compact objects occurs is thought to consist of an accretion disk, surrounded by a hot plasma, dubbed the corona (see e.g. Pringle 1981 for a review). Such a geometry can successfully explain the broad and varied properties of both accreting stellar mass black holes (Remillard & McClintock 2006) and active galactic nuclei (AGN; e.g. Done et al. 2012). Which component is energetically dominant, as well as the detailed structure of the accretion flow, depend principally on the accretion rate normalised to the Eddington rate \dot{m} (Abramowicz & Fragile 2013). Sources accreting at different \dot{m} are expected to have different disk structures, depending on the dominant cooling mechanism (radiation or advection of heat). Correlation studies between the X-ray spectral state, the two-point UV–X-ray spectral index α_{OX} and luminosity Eddington ratio (as a proxy for \dot{m}) have been used to constrain the dominant physical mechanisms regulating the accretion flow (e.g. Steffen 2006; Sobolewska et al. 2009).

Stars that are disrupted by the gravitational tidal forces of supermassive black holes (SMBHs; Hills 1975; Rees 1988) are signposts for extreme mass accretion rate variability. In such events, called tidal disruption events (TDEs), \dot{m} increases from (generally) neg-

ligible to potentially super Eddington rates in a matter of \sim weeks. Their subsequent evolution is observable for \sim months – years (e.g. Auchettl et al. 2017; van Velzen et al. 2020). After disruption, stream-stream collisions are thought to dissipate orbital angular momentum and energy, leading to the formation of an accretion disk (Rees 1988). Depending on the specific orbital dynamics this process may start after a few stream orbital windings (e.g. Bonnerot et al. 2016), or it may be inefficient (e.g. Shiohara et al. 2015). Observations of bright X-ray emission close to the UV/optical peak as well as optical spectral signatures suggests that at least in some cases, disk formation occurs quickly after disruption (Wevers et al. 2019b; Short et al. 2020).

The detection of late time UV emission (5–10 years after optical peak) suggests that TDE accretion disks are relatively stable and long-lived configurations (van Velzen et al. 2019). The UV and X-ray lightcurve of the TDE ASASSN–14li can be well modeled by a relativistic thin accretion disk at late times, suggesting that the bulk of the luminosity indeed originates from such a structure (Mummery & Balbus 2020). In addition, X-ray spectral variations (Komossa et al. 2004; Maksym et al. 2014), supported by more recent late time X-ray detections (Jonker et al. 2020), provide robust evidence that some TDEs undergo accretion state transitions. Jonker et al. (2020) also propose that the X-ray bright phase can be delayed with respect to the UV/optical peak,

^{*} E-mail: tw@ast.cam.ac.uk

which helps to explain the different L_{opt}/L_X ratios between optical and X-ray selected TDEs. Quantifying such differences provides important input when deriving TDE rates, luminosity and BH mass functions.

In this Letter, we analyse multi-wavelength data of 7 X-ray bright TDEs (Section 2). We present new correlations between their UV and X-ray properties in Section 3. These correlations can be interpreted as distinct accretion states/geometries, depending on their Eddington ratio, analogous to X-ray binaries and active galactic nuclei. We find that X-ray selected TDEs are more likely to be discovered at low Eddington ratio, while UV/optical selected TDEs are preferentially discovered at high Eddington ratios. We discuss these results and their implications, in particular differences in population properties depending on selection technique, in Section 4. We summarise the main take-away points in Section 5.

2 OBSERVATIONS

We search the literature for X-ray bright TDEs with sufficiently good quality X-ray data and UV coverage. We find 10 candidates, of which 3 (AT 2018zr, AT 2018hyz, AT 2019dsg) are excluded on the basis of short lightcurves (< 5 data points) and poor data quality. The resulting sample of 7 TDEs is listed in Table 1, and consists of 4 optical and 3 X-ray selected sources.

2.1 UV and X-ray observations

We use *Swift* X-ray Telescope (XRT) and UV/Optical Telescope (UVOT) observations to create lightcurves and stacked spectra for each source. UV fluxes are measured using the *wvotsource* task in HEASOFT (V6.24), using a $5''$ aperture and correcting for Galactic extinction using the dust map from Schlafly & Finkbeiner (2011). Given that TDEs remain significantly UV bright for 5–10 years after UV/optical peak (van Velzen et al. 2019), we do not correct for host galaxy contamination. We use simultaneous *Swift* UV+U band observations to fit a blackbody model to determine the average UV temperatures, assuming a flat temperature prior $4 < \log(T) < 4.7$. Distances are based on optical spectroscopic redshifts, assuming $H_0=70 \text{ km s}^{-1} \text{ Mpc}^{-1}$ and $\Omega_m=0.3$.

The X-ray count rates are obtained following the steps outlined in Evans et al. (2009), using the online *Swift*/XRT pipeline tool. Count rates are converted to X-ray fluxes using conversion factors depending on the X-ray spectral shape (see Table 1). Stacked spectra are created using the same *Swift*/XRT pipeline; they are binned to a minimum of 20 counts per bin, appropriate for using χ^2 statistics to assess goodness of fit. In case the X-ray spectrum changes over time (assessed by first investigating stacked spectra in smaller time bins), we derive multiple conversion factors appropriate for each lightcurve segment.

To estimate the relative strength of the thermal and power-law components in the X-ray spectra, we use a phenomenological 2-component spectral model in XSPEC: TBabs \times zshifit \times cflux \times (diskbb + powerlaw). The hydrogen column density is fixed to the Galactic foreground values from HI4PI Collaboration et al. (2016), and uncertainties are computed using the ERROR command. Our goal is not to provide the absolute best fit for each individual object (i.e. a different model may have a lower reduced χ^2 , χ_r), but to adopt a systematic approach to ensure simplicity as well as allowing a direct comparison between the quantities of interest across our sample. We

do note that the fits are generally statistically acceptable ($\chi_r < 1.3$), although some best fit models have $1.3 < \chi_r < 1.4$.

After fitting the stacked *Swift*/XRT spectra, we convert the observed countrates to fluxes (0.3–10 keV) using the best fit spectral parameters. We then use the best fit spectral model to assess the fractional contribution of each spectral component to the total flux; the power law contribution is subsequently used to estimate the monochromatic 2 keV X-ray flux ($L_{2 \text{ keV}}$), using the best fit indices from either the *Swift*/XRT stacked spectra or from the literature (if based on better quality *XMM-Newton* spectra; Table 1). Given the low blackbody temperatures, the power law component dominates the X-ray flux at 2 keV at all times. Uncertainties are propagated using standard conventions.

Finally, we calculate the UV to X-ray spectral slope α_{ox} following Tananbaum et al. (1979)

$$\alpha_{\text{ox}} = 1 - \frac{\log_{10}(\lambda L_{2500}) - \log_{10}(\lambda L_{2 \text{ keV}})}{\log_{10}(\nu_{2500}) - \log_{10}(\nu_{2 \text{ keV}})} \quad (1)$$

We use the UVW1 fluxes ($\lambda_{\text{cen}} = 2629 \text{ \AA}$) as a proxy for L_{2500} .

2.2 Black hole masses and Eddington ratios

Optical spectroscopic observations were obtained with the William Herschel (ISIS) and Magellan (MagE) telescopes (details can be found in Table A1), and reduced using IRAF or the CarPY software (Kelson 2003). All spectra are normalised to the continuum by fitting a low order spline function while masking absorption and emission lines. Following the procedure outlined in Wevers et al. (2017), we use the Penalised Pixel Fitting routine PPXF to measure the velocity dispersion of the spectra (Cappellari 2017).

We take these velocity dispersion measurements, as well as values from Wevers et al. (2019a) for ASASSN-15oi and XMMSL2J1446, and use the $M-\sigma$ relation of Gültekin et al. (2009) (including both early and late type galaxies) to convert them to black hole masses. Uncertainties are obtained by linearly combining the intrinsic scatter in the relation with the statistical (measurement) uncertainties in the velocity dispersions. For AT 2019ehz, we use SDSS and Pan-STARRS1 PSF and Petrosian/Kron fluxes to estimate a bulge-to-total correction of $(B/T)_g = 0.23$. We combine this with the galaxy stellar mass from van Velzen et al. (2020) and the $M_{\text{BH}} - M_{\text{bulge}}$ relation of Häring & Rix (2004) to estimate the black hole mass. Including an intrinsic scatter of 0.3 dex and a factor 0.2 dex uncertainty in the bulge mass, this yields $\log_{10}(M_{\text{BH}}) = 6.1^{+0.5}_{-0.5} M_{\odot}$.

The Eddington luminosity is calculated as $L_{\text{Edd}} = 1.26 \times 10^{38} M_{\text{BH}} \text{ erg s}^{-1}$. To account for the fact that the UVW1 filter is on the Rayleigh-Jeans tail of the blackbody emission (Table 1), we apply a temperature correction (see van Velzen et al. 2019) to obtain the UV luminosity L_{UV} (not to be confused with L_{UVW1}), and define Eddington ratios $f_{\text{Edd,UV}} \equiv L_{\text{UV}}/L_{\text{Edd}}$ and $f_{\text{Edd,X}} \equiv L_X/L_{\text{Edd}}$. To account for the potentially important contribution of the X-ray emission at EUV wavelengths, we find the bolometric luminosity by extrapolating the X-ray spectral model into the energy range 0.01–10 keV and adding L_{UV} , such that $f_{\text{Edd,bol}} \equiv (L_{0.01-10 \text{ keV}} + L_{\text{UV}})/L_{\text{Edd}}$. Uncertainties in f_{Edd} include both the black hole mass and photometric measurement uncertainties, with the former being dominant.

Table 1. Overview of the parameters adopted for the analysis. We provide the X-ray spectral model parameters based on the *Swift*/XRT stacked spectra, including temperature kT , power law index Γ , the relative contribution of the power law to the total X-ray flux (0.3–10 keV; PL frac) and the X-ray luminosity (0.3–10 keV) at UV peak. Values marked with an asterisk are frozen to best-fit values obtained from *XMM-Newton* observations. References are listed below the table. We also provide the assumed distance (D_{lum} , measured velocity dispersion σ , derived M_{BH} , and the peak UV luminosity, the average (bolometric) Eddington ratio and average α_{ox} . Multiple entries indicate multiple epochs with significantly different properties (see Table A2).

| Source | kT eV | Γ | PL frac | D_{lum} Mpc | L_X 10^{43} erg s $^{-1}$ | σ km s $^{-1}$ | M_{BH} $\log_{10}(M_{\odot})$ | L_{UV} 10^{43} erg s $^{-1}$ | T_{BB} $\log_{10}(\text{K})$ | $\langle f_{\text{Edd,bol}} \rangle$ | $\langle \alpha_{\text{ox}} \rangle$ |
|--------------------------|-------------------|-----------------|------------------------|-------------------------|----------------------------------|--------------------------|---|--|--|--------------------------------------|--------------------------------------|
| ASASSN–15oi ^a | 47* | 2.5* | $0.07^{+0.25}_{-0.07}$ | 215 | 0.5 ± 0.2 | 61 ± 7 | 5.93 ± 0.60 | 10.3 ± 0.3 | 4.45^a | –0.03 | 2.09 |
| | 42* | 3.3* | 0.02 | | | | | | | 0.20 | 2.31 |
| AT 2019azh ^b | 59 ± 11 | 2.6 ± 1.1 | 0.20 ± 0.20 | 96 | 0.08 ± 0.05 | 77 ± 2 | 6.36 ± 0.43 | 28.0 ± 0.5 | 4.51^h | –0.24 | 2.54 |
| | 55 ± 3 | 5.9 ± 1.2 | $0.29^{+0.16}_{-0.25}$ | | | | | | | –0.57 | 2.75 |
| AT 2019ehz ^c | 138^{+15}_{-12} | 2.8 ± 1 | $0.05^{+0.3}_{-0.05}$ | 335 | 6.2 ± 0.4 | — | 6.10 ± 0.50 | 9.7 ± 0.5 | 4.34^h | –0.50 | 2.09 |
| AT 2018fyk ^d | 142 ± 10 | 2.8 ± 1 | 0.25 ± 0.13 | 264 | 13.3 ± 0.7 | 158 ± 1 | 7.69 ± 0.39 | 48 ± 2 | 4.63 | –1.11 | 1.91 |
| | 179 ± 8 | 2.20 ± 0.08 | 0.68 ± 0.04 | | | | | | | –1.89 | 1.22 |
| XMMSL1J0740 ^e | 207 ± 27 | 1.95 ± 0.29 | 0.59 ± 0.11 | 75 | 0.48 ± 0.03 | 112 ± 3 | 7.05 ± 0.43 | 0.62 ± 0.01 | 4.24 | –2.33 | 1.55 |
| XMMSL2J1446 ^f | 113* | 2.58* | 0.87* | 127 | 0.37 ± 0.05 | 167 ± 15 | 7.79 ± 0.55 | 0.33 ± 0.01 | 4.15 | –2.61 | 1.44 |
| XMMSL1J1404 ^g | 123 ± 10 | 2.7 ± 0.33 | $0.38^{+0.13}_{-0.09}$ | 190 | 3.0 ± 0.3 | 93 ± 1 | 6.71 ± 0.40 | 0.29 ± 0.05 | 4.22 | –0.90 | 1.25 |

^aHoloien et al. (2016); ^bGezari et al. (2017), ^b aka ASASSN–19dj, Liu et al. (2019), ^c aka Gaia19bpt, van Velzen et al. (2020), ^d aka ASASSN–18ul, Wevers et al. (2019b), ^e Saxton et al. (2017) ^f Saxton et al. (2019), ^g Saxton et al., in prep., ^h van Velzen et al. (2020)

3 ANALYSIS AND RESULTS

3.1 Correlation analysis

Power law correlations between several variables such as α_{ox} , $L_{2 \text{ keV}}$, Γ and Eddington ratio have been found in the active SMBH population (Steffen 2006; Vasudevan & Fabian 2007; Lusso et al. 2010). Therefore, we investigate possible correlations between observables in log space, using a hierarchical Bayesian approach to linear regression (LINMIX). This method allows to take into account heteroscedastic measurement errors and covariances (Kelly 2007).

We report a strong, statistically significant correlation between α_{ox} and $f_{\text{Edd,bol}}$. The best fit regression line (Figure 1) is given by

$$\alpha_{\text{ox}} = (3.03 \pm 0.11) + (1.08 \pm 0.08) \log_{10}(f_{\text{Edd,bol}}) \quad (2)$$

quoting posterior distribution median estimates, and the uncertainties are the standard deviations of the posteriors. The correlation coefficient is constrained to $\hat{\rho} > 0.95$. The effect of systematic uncertainties in the M – σ relation is assessed by sampling each M_{BH} within its uncertainty, and performing the linear regression using the resulting $f_{\text{Edd,bol}}$ values. Using 200 trials, we find identical results, but with a scatter ~ 5 times larger than the statistical uncertainties.

The observed $\alpha_{\text{ox}} - f_{\text{Edd,bol}}$ correlation is likely driven by a strong negative correlation between $L_{2 \text{ keV}}$ and $f_{\text{Edd,UV}}$, such that the 2 keV X-ray emission is weaker when $f_{\text{Edd,UV}}$ is higher (Fig. 1, bottom right panel):

$$L_{2 \text{ keV}} = (37.0 \pm 0.3) - (2.58 \pm 0.18) \log_{10}(f_{\text{Edd,UV}}) \quad (3)$$

The correlation coefficient is constrained to $\hat{\rho} = -0.87 \pm 0.02$.

Finally, we report a correlation between $f_{\text{Edd,X}}$ and $f_{\text{Edd,UV}}$, with $\hat{\rho} = 0.78 \pm 0.10$ (Figure 1, lower left panel):

$$f_{\text{Edd,X}} = (-0.43 \pm 0.23) + (0.78 \pm 0.13) \log_{10}(f_{\text{Edd,UV}}) \quad (4)$$

These correlations remain statistically significant (10, 10 and 6 σ respectively) when removing AT 2018fyk from the sample.

We note that we also recover the canonical $L_{\text{UV}} - L_{2 \text{ keV}}$ relation seen in AGN (Lusso & Risaliti 2016), although the correlation coefficient is weak ($\hat{\rho} = 0.34 \pm 0.05$). We find $\hat{\alpha} = 10.6 \pm 5.2$, $\hat{\beta} = 0.70 \pm 0.12$, fully consistent with the Lusso & Risaliti (2016) relation

– albeit with much larger scatter in the parameters due to the small sample size.

3.2 X-ray spectral state as a function of $f_{\text{Edd,bol}}$

The results of our X-ray spectral fitting are provided in Table 1. We find that broadly speaking, the TDEs in our sample can be divided into blackbody or power law dominated spectral states. The former sources have on average higher α_{ox} values (2.28 ± 0.32), lower power law fractions (0.17 ± 0.12), as well as somewhat steeper power law indices, and are found at $f_{\text{Edd,bol}} \gtrsim 0.03$. The power law dominated sources have lower α_{ox} values (1.33 ± 0.17), higher power law fractions (0.63 ± 0.18), shallower power law indices and are found at $f_{\text{Edd,bol}} \lesssim 0.03$. This transition value of $f_{\text{Edd,bol}}$ is subject to considerable uncertainties, dominated by the intrinsic scatter in the M – σ relation.

The average black hole masses for the blackbody and power law dominated spectral states are mutually compatible within the typical uncertainty, although the sample size is small and thence the scatter large.

4 DISCUSSION

4.1 Potential contamination of α_{ox}

Mummery & Balbus (2020) showed that at very early times there may be significant contamination from an additional, exponentially decaying energy source at UV wavelengths (in excess of the disk emission). This emission decays in ≈ 200 days for ASASSN–14li. Similar behaviour likely occurs for most UV/optical discovered TDEs, given their similar lightcurve evolution and properties (e.g. Hinkle et al. 2020; van Velzen et al. 2020).

As a result, our α_{ox} values at early times may be similarly contaminated due to UV emission unrelated to the disk. However, Figure 1 (top panel) shows that even the *late time* emission in ASASSN–15oi and AT 2019azh (observed ~ 250 days after the UV peak, after the relatively large gaps in the $f_{\text{Edd,bol}}$ evolution) has a

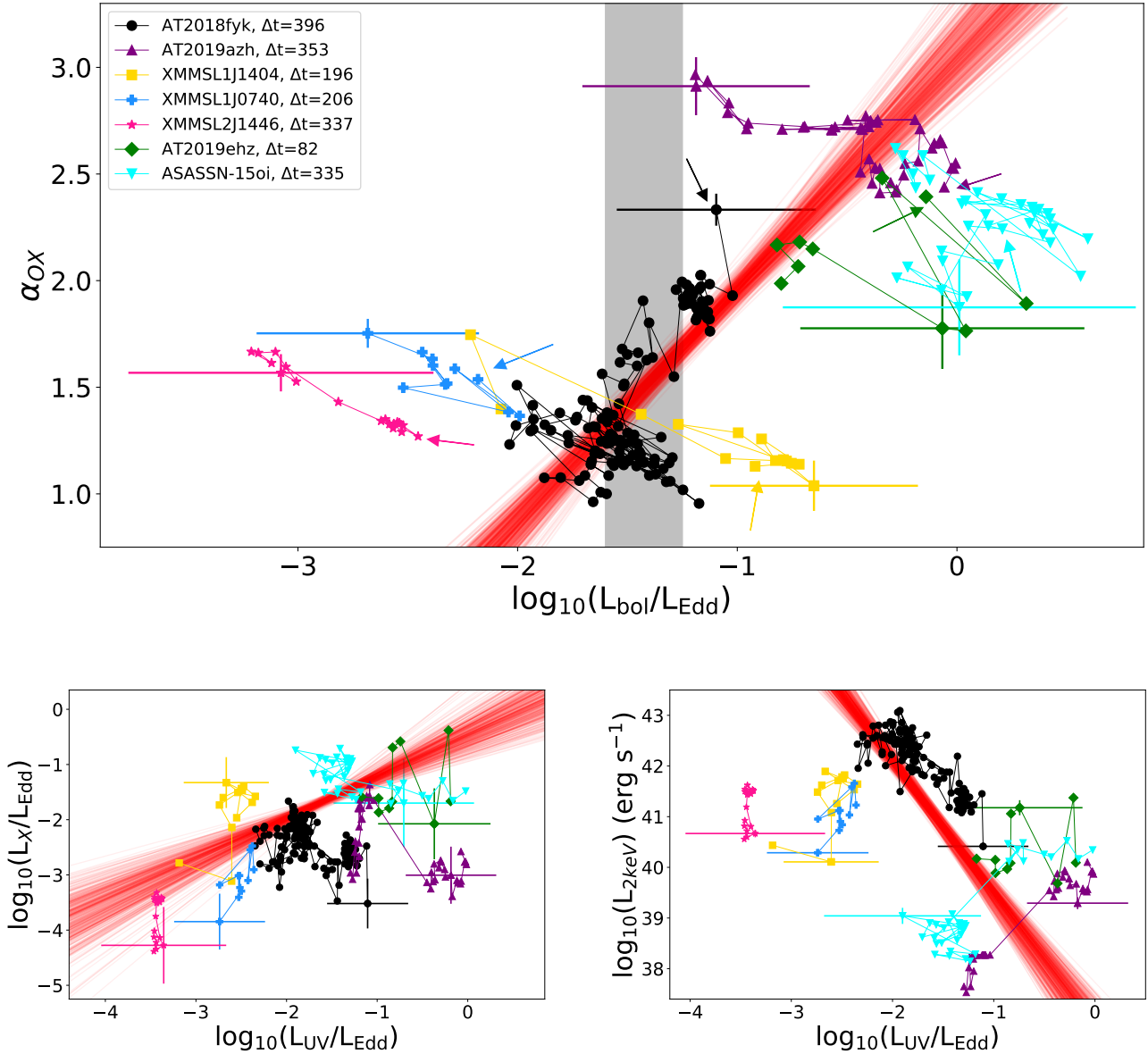


Figure 1. Top: UV to X-ray spectral slope (α_{OX}) as a function of $f_{Edd,bol}$. Red lines are samples drawn from the posterior distributions of the best fit regression line. The black shaded region indicates the approximate division between disk-dominated (higher f_{Edd}) and power-law dominated (lower f_{Edd}) X-ray spectra. The first observation is marked by a coloured arrow to indicate the time evolution; Δt is the lightcurve duration, in days. We show the median error bar for each source. Bottom left: best fit regression line between $f_{Edd,X}$ and $f_{Edd,UV}$. Bottom right: best fit regression line between $L_{2\text{ keV}}$ and $f_{Edd,UV}$.

significantly higher α_{OX} than the X-ray selected sources. The fact that these late time data are closer to the regression line may indicate that some contamination is indeed present at early times. Nevertheless, their X-ray spectra have similar properties at *all* times, and in the case of ASASSN–15oi, narrow Fe II emission indicates that we are observing the disk directly at late times, also in optical light (Wevers et al. 2019b). Removing the low X-ray luminosity data (close to UV/optical peak) for ASASSN–15oi and AT 2019azh steepens the $L_{2\text{ keV}}-f_{Edd,UV}$ correlation ($\hat{\alpha}=38.05\pm 0.25$ and $\hat{\beta}=-2.14\pm 0.15$).

There is no evidence for systematically higher gas column densities in the X-ray spectra of the high α_{OX} sources (e.g. Auchettl et al. 2017). Barring extreme gas-to-dust ratios, this also implies that systematically higher dust obscuration in the UV for the low

α_{OX} sources is disfavoured. We also note that including potential host galaxy contamination in the relatively UV faint X-ray selected TDEs would make the distinction in α_{OX} more pronounced, as they would be intrinsically more X-ray strong (i.e. move to lower α_{OX}).

4.2 Accretion state transitions as a function of $f_{Edd,bol}$

Our analysis shows that sources at higher Eddington ratio have higher α_{OX} values, i.e. their 2 keV X-ray luminosity is weaker for their Eddington scaled UV luminosity. In Figure 1 we have provided a tentative shaded region to guide the eye; sources to the right of this region (around $f_{Edd,bol} \approx 0.03$) all have X-ray spectra dominated by

a thermal component (Table 1). Sources on the left of this region have an X-ray spectrum dominated by a power law.

In AGN there is evidence for correlations similar to those presented here (Steffen 2006; Vasudevan & Fabian 2007; Lusso et al. 2010). Moreover, marked changes in X-ray spectral state and SED appear to coincide with sources crossing a *transition* value of $f_{\text{Edd,bol}} \sim 0.02$ in both AGN and XRBs (Maccarone et al. 2003; Remillard & McClintock 2006), although with large scatter in some cases (Maccarone 2003). We find, encouragingly, that the transition occurs at very similar values in TDEs. While several attempts to explain the observed correlations with simple models for AGN accretion flows exist (Kubota & Done 2018; Arcodia et al. 2019), it remains unclear what the dominant physical mechanism to explain the interplay between the disk and corona is.

The strong negative correlation observed between $L_{2\text{ keV}}$ and $f_{\text{Edd,UV}}$ shows that a mechanism regulating the energetic interaction between the corona and UV photon field must exist. Although other sources of UV radiation (e.g. the exponentially declining component reported in Mummery & Balbus 2020) may also play a role, we note that the UV blackbody component at peak in TDEs is produced at radii much larger than the putative accretion disk (Wevers et al. 2019a). Systematic uncertainties in M_{BH} also do not appear to explain the observed behaviour. We do note that the most massive sources are all observed in the hard state, which may indicate that their evolution is faster than TDEs around low mass black holes.

The apparent flattening of α_{ox} at very high and very low $f_{\text{Edd,bol}}$ may instead reflect changes in disk structure and/or dominant emission mechanism. At low $f_{\text{Edd,bol}}$, a transition from a thin disk to an advection dominated accretion flow will lead to softer emission, potentially through a shift in dominant X-ray emission mechanism, or changes in radiative transfer in the disk photosphere (see e.g. Ruan 2019, and references there-in). There is some evidence of this process occurring in XMMSL2J1446 (Fig. 1). At high $f_{\text{Edd,bol}}$, a transition to a slim disk may prevent arbitrarily soft α_{ox} due to an increased scale height and/or advective cooling.

4.3 Potential selection effects in X-ray surveys

Given that the properties of both the X-ray and optically selected TDEs are consistent with the state transition scenario, it seems unlikely that the X-ray selected TDEs are probing an intrinsically different class of objects. Moreover, there are no significant differences between X-ray and optically selected TDE host black hole masses (Wevers et al. 2019a), although the sample size prevents robust conclusions (French et al. 2020). The low observed peak UV luminosities of the X-ray selected TDEs open the possibility that the observed X-ray emission is significantly delayed with respect to the UV/optical peak of the lightcurve. This scenario was recently proposed by Jonker et al. (2020) to explain the differences in $L_{\text{opt}}/L_{\text{X}}$ of optical and X-ray selected TDEs.

A physically motivated explanation could be a viscous delay between disruption and the onset of accretion, where material is unable to circularise efficiently, delaying the emergence of accretion powered emission (Guillochon & Ramirez-Ruiz 2015). This scenario was invoked by Gezari et al. (2017) to explain the behaviour of ASASSN–15oi, and later also for AT 2019azh (Liu et al. 2019). In these sources, the X-ray emission is observed to increase over a period of ~ 250 days, while the UV emission fades. These two sources were discovered at optical wavelengths close to UV/optical peak, and are therefore observed at high $f_{\text{Edd,bol}}$. The properties of the X-ray selected TDEs are compatible with a similar evolution, provided that we missed the peak of the UV/optical emission. On

the other hand, they do show significant evolution over time (Saxton et al. 2017), suggesting that the gap is likely not more than about a year. An alternative scenario with a time-variable absorbing column density (higher at early times due e.g. to an increased scale height of the inner disk or a wind), can also explain the observed properties (Wen et al. 2020).

The X-ray selected sources in our sample appear to have been detected when they were very X-ray strong (low α_{ox}). Taking into consideration the delayed accretion scenario as well as the discovered correlations with $f_{\text{Edd,bol}}$ and $f_{\text{Edd,UV}}$, this will result in X-ray surveys preferentially detecting TDEs at lower Eddington ratios and α_{ox} , well after the UV/optical peak. As a caveat we note that the selection function also depends on survey cadence and duration of the X-ray peak of the lightcurve, which is not well constrained at present. Nevertheless, a sample of X-ray bright, optical selected TDEs combined with X-ray selected TDEs will cover the full range of Eddington ratios from $\sim 10^{-4} - 1$ (see Figure 1), which are of interest to study accretion state transitions in SMBHs.

5 CONCLUSIONS

We summarise our main findings below:

- Using 7 TDEs we find statistically significant correlations between α_{ox} , $f_{\text{Edd,X}}$ and Eddington ratio, as well as an anti-correlation between $L_{2\text{ keV}}$ and $f_{\text{Edd,UV}}$. Using linear regression, we find slopes inconsistent with 0 at the 14, 14 and 6 σ level, respectively. The emission significantly softens at higher Eddington ratio; in other words, the power law X-ray emission is suppressed more rapidly than the UV luminosity when moving to higher $f_{\text{Edd,bol}}$.
- We find that on average, sources at higher $f_{\text{Edd,bol}}$ have disk dominated X-ray spectra, with high α_{ox} values and a small power law contribution to the total X-ray flux. Sources at lower $f_{\text{Edd,bol}}$ have power law dominated X-ray spectra and lower α_{ox} values. A spectral state transition occurs around $f_{\text{Edd,bol}} \sim 0.03$, although there is significant uncertainty in this value, due to the small sample size and M_{BH} uncertainties. TDEs around the most massive SMBHs are observed in the hard state; this could indicate that TDE evolution is faster around more massive black holes.
- Our results show that the UV and X-ray properties of optical and X-ray selected TDEs can differ significantly. Such selection effects must be taken into account when computing TDE rates, luminosity and BH mass functions, particularly in the X-ray band.
- The small sample used here covers Eddington ratios spanning 4 orders of magnitude, from 10^{-4} to 1. We find both qualitative and quantitative similarities with XRB and AGN accretion flows. The rapid evolution from Eddington limited to low accretion rates makes TDEs promising tools to study changes in accretion flow structure in individual SMBHs.
- The X-ray emission appears to be delayed with respect to the UV/optical peak for several optical TDEs (Jonker et al. 2020). In combination with the reported correlations, this implies that X-ray surveys are more likely to find TDEs in the low Eddington accretion regime, while UV/optical surveys are more sensitive to the high Eddington regime. Combining X-ray and optical samples will provide the best leverage in studying accretion properties over

a large range of f_{Edd} .

Large samples of TDEs detected with current and future X-ray and optical surveys will allow statistical studies of the accretion flow formation, properties and evolution (e.g. disk-corona geometry and interplay), providing new insights into the fundamental physics governing accretion in black holes.

ACKNOWLEDGEMENTS

I thank Matt Auger, Peter Jonker, Dom Walton and Martha Irene Saladino for insightful comments and discussions; the referee, Richard Saxton, for astute comments and suggestions in prompt and constructive reports; and DJ Pasham and Ani Chiti for performing the Magellan observations. This work is funded by ERC grant 320360 and European Commission grant 730980. We acknowledge the use of public data from the *Swift* data archive. This paper includes data gathered with the 6.5 meter Magellan Telescopes located at Las Campanas Observatory, Chile, as well as observations obtained with the William Herschel Telescope (proposal ID: W19B/P7) operated on the island of La Palma by the Isaac Newton Group of Telescopes in the Spanish Observatorio del Roque de los Muchachos of the Instituto de Astrofísica de Canarias.

REFERENCES

- Abramowicz M. A., Fragile P. C., 2013, *Living Reviews in Relativity*, **16**, 1
 Arcodia R., Merloni A., Nandra K., Ponti G., 2019, *A&A*, **628**, A135
 Auchettl K., Guillochon J., Ramirez-Ruiz E., 2017, *ApJ*, **838**, 149
 Bonnerot C., Rossi E. M., Lodato G., Price D. J., 2016, *MNRAS*, **455**, 2253
 Cappellari M., 2017, *MNRAS*, **466**, 798
 Done C., Davis S. W., Jin C., Blaes O., Ward M., 2012, *MNRAS*, **420**, 1848
 Evans P. A., et al., 2009, *MNRAS*, **397**, 1177
 French K. D., Wevers T., Law-Smith J., Graur O., Zabludoff A. I., 2020, *Space Sci. Rev.*, **216**, 32
 Gezari S., Cenko S. B., Arcavi I., 2017, *ApJ*, **851**, L47
 Guillochon J., Ramirez-Ruiz E., 2015, *ApJ*, **809**, 166
 Gültekin K., et al., 2009, *ApJ*, **698**, 198
 HI4PI Collaboration et al., 2016, *A&A*, **594**, A116
 Häring N., Rix H.-W., 2004, *ApJ*, **604**, L89
 Hills J. G., 1975, *Nature*, **254**, 295
 Hinkle J. T., Holoien T. W. S., Shappee B. J., Auchettl K., Kochanek C. S., Stanek K. Z., Payne A. V., Thompson T. A., 2020, *ApJ*, **894**, L10
 Holoien T. W. S., et al., 2016, *MNRAS*, **455**, 2918
 Jonker P. G., Stone N. C., Genozov A., Velzen S. v., Metzger B., 2020, *ApJ*, **889**, 166
 Kelly B. C., 2007, *ApJ*, **665**, 1489
 Kelson D. D., 2003, *PASP*, **115**, 688
 Komossa S., Halpern J., Scharnt N., Hasinger G., Santos-Lleo M., Predehl P., 2004, *ApJ*, **603**, L17
 Kubota A., Done C., 2018, *MNRAS*, **480**, 1247
 Liu X.-L., Dou L.-M., Shen R.-F., Chen J.-H., 2019, arXiv e-prints, p. arXiv:1912.06081
 Lusso E., Risaliti G., 2016, *ApJ*, **819**, 154
 Lusso E., et al., 2010, *A&A*, **512**, A34
 Maccarone T. J., 2003, *A&A*, **409**, 697
 Maccarone T. J., Gallo E., Fender R., 2003, *MNRAS*, **345**, L19
 Maksym W. P., Lin D., Irwin J. A., 2014, *ApJ*, **792**, L29
 Mummery A., Balbus S. A., 2020, *MNRAS*, **492**, 5655
 Pringle J. E., 1981, *ARA&A*, **19**, 137
 Rees M. J., 1988, *Nature*, **333**, 523
 Remillard R. A., McClintock J. E., 2006, *ARA&A*, **44**, 49
 Ruan J. J. e. a., 2019, *ApJ*, **883**, 76

Table A1. Observing log of the optical spectroscopy. The slit width was 0.7 arcsec for all observations. The observations of AT 2018fyk were seeing-limited, resulting in a better spectral resolution.

| Name | Instr | Exp. time sec | σ_{instr} km s ⁻¹ | Obs. date |
|-------------|-----------|------------------|--|------------|
| AT 2018fyk | MagE | 2x1800 | 17 | 2019/08/13 |
| AT 2019azh | ISIS/R600 | 2700 | 45 | 2020/02/02 |
| XMMSL1J0740 | MagE | 800 | 22 | 2020/02/15 |
| XMMSL1J1404 | MagE | 2700 | 22 | 2020/02/15 |

Table A2. Julian date range for each epoch referenced in Table 1.

| Name | MJD days |
|-------------|--------------------------------|
| ASASSN-15oi | 57 276-57 340 57 468-57 611 |
| AT2019azh | 58 553-58 635 58 767-58 906 |
| AT2019ehz | 58 620-58 702 |
| AT2018fyk | 58 383-58 447 58 579-58 779 |
| XMMSL1J0740 | 56 782-56 988 |
| XMMSL2J1446 | 57 643-57 980 |
| XMMSL1J1404 | 58 177-58 373 |

- Saxton R. D., Read A. M., Komossa S., Lira P., Alexander K. D., Wieringa M. H., 2017, *A&A*, **598**, A29
 Saxton R. D., et al., 2019, *A&A*, **630**, A98
 Schlafly E. F., Finkbeiner D. P., 2011, *ApJ*, **737**, 103
 Shiokawa H., Krolik J. H., Cheng R. M., Piran T., Noble S. C., 2015, *ApJ*, **804**, 85
 Short P., et al., 2020, arXiv e-prints, p. arXiv:2003.05470
 Sobolewska M. A., Gierliński M., Siemiginowska A., 2009, *MNRAS*, **394**, 1640
 Steffen A. T. e. a., 2006, *AJ*, **131**, 2826
 Tananbaum H., et al., 1979, *ApJ*, **234**, L9
 Vasudevan R. V., Fabian A. C., 2007, *MNRAS*, **381**, 1235
 Wen S., Jonker P. G., Stone N. C., Zabludoff A. I., Psaltis D., 2020, arXiv e-prints, p. arXiv:2003.12583
 Wevers T., van Velzen S., Jonker P. G., Stone N. C., Hung T., Onori F., Gezari S., Blagorodnova N., 2017, *MNRAS*, **471**, 1694
 Wevers T., et al., 2019a, *MNRAS*, **487**, 4136
 Wevers T., et al., 2019b, *MNRAS*, **488**, 4816
 van Velzen S., Stone N. C., Metzger B. D., Gezari S., Brown T. M., Fruchter A. S., 2019, *ApJ*, **878**, 82
 van Velzen S., et al., 2020, arXiv e-prints, p. arXiv:2001.01409

APPENDIX A: OBSERVING LOG AND ADDITIONAL INFORMATION